Advanced Steel Construction – Vol. 21 No. 6 (2025) 551–560
DOI:10.18057/IJASC.2025.21.6.8

ESTIMATION OF DEFORMATION CAPACITY OF CIRCULAR HOLLOW SECTION BASED ON STRAIN

Heng-Li Fu [1, 2], Gan-Ping Shu [1, 2, *], Jin Zhang [3], Bao-Feng Zheng [1, 2], Li-Bo Wang [1, 2] and Zhan-Peng Chen [1, 2]

[1] *Key Laboratory of Concrete and Prestressed Concrete Structures of Ministry of Education, Southeast University, Nanjing 210096, China*
[2] *School of Civil Engineering, Southeast University, Nanjing 210096, China*
[3] *ARTS Group Co., Ltd., Suzhou 215123, China*
** (Corresponding author: E-mail: shuganping@seu.edu.cn)*

ABSTRACT

The deformation evaluation of steel members is an important part of the performance-based seismic design of steel structures. The strain-based deformation capacity is not susceptible to load and boundary conditions, and can directly reflect the ductility of the component. According to the mechanical properties of steel circular hollow section (CHS) beam-columns in engineering structures, this paper proposes a strain-based ductility coefficient derived from the equivalent plastic zone to estimate their deformation capacity. Six typical circular hollow section steel components were subjected to quasi-static tests, with different diameter-to-thickness ratio and axial compression ratio as the test parameters. Based on the experimental results, a validated and reliable finite element model was established to analyze the effects of various factors on the strain ductility coefficient of steel circular hollow sections under quasi-static loading. The results indicated that the strain ductility coefficient decreased with increasing diameter-to-thickness ratio and axial compression ratio. A recommended empirical formula for the strain ductility coefficient of circular hollow section beam-columns was proposed using regression analysis. The empirical formula has high accuracy, serving as a reference for promoting the application of performance-based seismic design in steel structures.

ARTICLE HISTORY

Received: 21 April 2025
Revised: 21 May 2025
Accepted: 26 May 2025

KEYWORDS

Quasi-static test;
Circular hollow section;
Strain ductility coefficient;
Performance-based seismic design

1. Introduction

In the past few decades, the focus of seismic design has shifted from "strength" to "performance" [1]. Performance-based seismic design is currently a hot topic in structural seismic research. Deformation is an important indicator for measuring structural performance levels, and the current performance-based design theory primarily emphasizes nonlinear deformation at both the structural and component levels. Circular hollow sections are commonly used as the main structural members due to their advantages such as high strength-to-weight ratio, excellent seismic performance, ease of construction, and controllable quality [2].Therefore, it is essential to accurately estimate their deformation capacity to ensure a rational seismic design of the overall structure.

Performance-based seismic design for engineering structures was first proposed by scholars from the United States and Japan in the 1990s [3]. In Japan, JACI 2000 defines performance objectives, explicitly specifying the performance standards that different types of buildings should achieve under earthquake action. It also sets different seismic performance targets for buildings based on varying levels of seismic intensity. The concept of performance-based seismic design was first formally introduced in the United States in 1995 through the publication of the document Vision 2000, which laid the foundation for the development of performance-based design methodologies [4]. FEMA 273 [5] was the first performance-based seismic design code, mainly outlining seismic performance objectives, performance classification, and design methods. In 2010, the United States issued the document TBI-2010 High-Rise Building Performance-Based Seismic Design Guidelines [6], a new performance-based seismic design method that provides clear performance evaluation criteria for the whole structure and its structural components. The structural design standards such as FEMA 356 [7], ASCE 41-13 [8] and ASCE 41-17 [9] also explain performance-based design. For the performance-based seismic design of steel structures, Chinese standards, Standard for design of steel structures (GB 50017-2017) [10] and Code for seismic design of buildings (GB/T 50011-2010) [11], provide relevant provisions. However, these codes primarily rely on load-bearing capacity checks and construction detailing requirements, without specifying deformation limits for different performance levels.

In recent years, extensive research has been carried out by scholars worldwide on the seismic behavior of structural members. Fan et al. [12] conducted static tests on three steel tubular columns with low axial compression ratios, mainly to investigate the effects of diameter-to-thickness ratio and axial compression ratio on the deformation performance of steel tubular columns. Xin et al. [13]conducted experimental and numerical investigations into the global buckling behaviour of circular hollow section (CHS) beam-columns fabricated from both normal and high strength structural steels, and proposed improved stability design approaches. Zheng et al. [14]conducted a study on the seismic behaviour of hot-rolled stainless steel circular hollow section (CHS) beam-columns. Their experimental findings revealed that these members primarily failed through local buckling at the ends, and demonstrated good seismic performance owing to the inherent ductility of stainless steel. Xing et al. [15]investigated the hysteretic performance of circular hollow section (CHS) steel members subjected to cyclic axial loads and lateral displacements. The results showed that, compared to tension-dominated members, those under various levels of compressive force exhibited more pronounced global deformations. Wang et al. [16] used finite element method to study the hysteretic properties such as ultimate bearing capacity, ductility coefficient and energy dissipation coefficient of circular steel pipe members to provide a basis for failure mechanism analysis of large-span space structures under seismic action. Mohamed Elchalakani et al. [17] conducted cyclic bending tests on cold-formed round tubes, mainly to investigate the effect of diameter-to-thickness and length-to-finish ratios on the ductility of the members and to derive the limiting values of length-to-finish ratios of the members applied to seismic design. Guo et al. [18] investigated the seismic performance of steel circular hollow section after being subjected to lateral impact loading, the test results showed that the impact height had a negative effect on the deformation capacity of steel circular hollow sections and proposed a simplified hysteresis model considering the effects of a combination of impact height and axial horizontal loading. Fang et al. [19] conducted an experimental study on the seismic performance of elliptical circular hollow section columns to investigate the effects of different tube thicknesses, axial compression ratios, and bending directions on the damage pattern, yield strength, and ductility of the members. Zhang et al. [20] proposed the use of strain-based ductility indices to enhance the applicability of the fiber model and developed an empirical formula for the strain ductility of H-shaped sections. At present, there are few studies on the deformation capacity of circular hollow section under different axial compression ratios.

In structural elastoplastic analysis, beam-column members are typically modeled using plastic hinge or fiber-based approaches. The deformation indices, rotation angle (θ) and curvature (φ), are primarily applied in the plastic hinge model. Meanwhile, for beam-column members, it is challenging to define the moment-rotation relationship while considering the coupling effect of moment and axial force. On the other hand, strain indices are more applicable to the fiber model. The yield strain (ε_y) is solely dependent on the material properties and is not influenced by the geometric characteristics of the member or loading boundary conditions. In elastoplastic analysis, the material strain response in the fiber model can be directly obtained. Therefore, evaluating the performance of steel members based on strain indices offers high applicability and convenience. At present, there are few studies on circular hollow sections based on deformation capacity under various axial pressure ratios. Therefore, a systematic study on the ductility of circular hollow sections is of reference

significance for improving the seismic performance-based evaluation criteria.

2. Experimental programme

2.1. Design principles

Steel frame is the most common steel structure system in engineering applications, which is mainly composed of frame columns and frame beams. Fig. 1 shows the stress form of typical steel frame under in-plane bending moment. The main mechanical characteristics of the frame column can be equivalent to the cantilever column component intercepted from the inflection point to the fixed end. Therefore, the cantilever column component is taken as the test component in this paper.

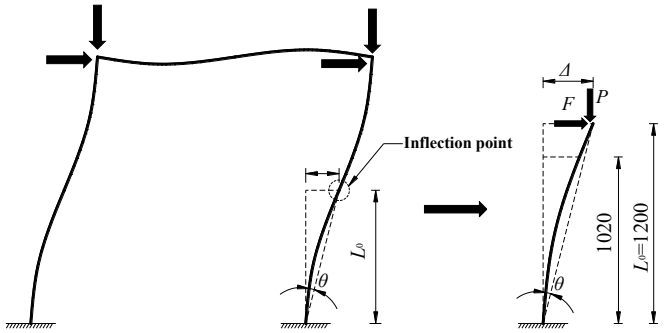

Fig. 1 typical steel frame and column equivalent cantilever members

2.2. Description of the components

Six Q355 circular hollow section components were tested under a combination of vertical load and cyclic horizontal displacement. The cross-section grades of the components in this study cover common engineering types, corresponding to cross-section grades 1 to 4 specified in the Chinese standard GB50017-2017 [10]. These grades are mainly determined by steel type and diameter-thickness ratio. In addition, axial compression ratios of 0.2, 0.4, and 0.6 were set to examine the effects of different axial compression ratios on the behavior of circular hollow sections. The nominal cross-sectional dimensions $D \times t$ (D and t represent the diameter and thickness of the CHS component, respectively) of the CHS component are 219 × 8, 219 × 6, 219 × 4 and 219 × 3.5. Due to the uncommon sizes of 219 × 4 and 219 × 3.5 circular hollow sections, this batch of CHS component was obtained by machining 219 × 6 the CHS component. The dimensions of each component are shown in Table 1. The cross-sectional schematic is shown in Fig. 2. The component labels in Table 1 consist of three parts, with the first part "S1", "S2", "S3", and "S4" representing cross-section grade 1, cross-section grade 2, cross-section grade 3, and cross-section grade 4, respectively. The "219 × 8" in the second part represents the nominal diameter and nominal thickness of the component section. The numbers "0.2", "0.4", and "0.6" in the third part represent different axial compression ratios n ($n=P/Af_y$), where P is the constant axial load applied and A is the measured cross-sectional area, f_y is the yield stress of steel. The fourth part represents the loading mode, where "C" represents loop loading. For example, component S1-219 × 8-0.2-C represents a circular hollow section with a cross-sectional grade of 1, a cross-sectional diameter of 219mm, a thickness of 8mm, and an axial compression ratio of 0.2, subjected to cyclic loading.

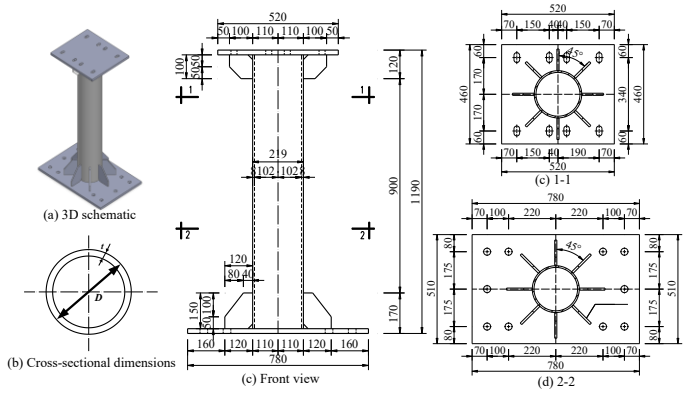

Fig. 2 Details of test component A-C-219×8-0.2 (unit: mm)

Table 1
Main design parameters of test components

Component number	Grade	D(mm)	t(mm)	n	D/t	Cross-section Grade
A-C-219×8-0.2	355	219	8	0.2	27.375	S1
A-C-219×8-0.4	355	219	8	0.4	27.375	S1
A-C-219×8-0.6	355	219	8	0.6	27.375	S1
A-C-219×6-0.2	355	219	6	0.2	36.5	S2
A-C-219×4-0.2	355	219	4	0.2	54.75	S3
A-C-219×3.5-0.2	355	219	3.5	0.2	63	S4

In order to avoid the influence of weld seams and enable more direct observation of the failure modes and deformation capacity of circular steel members, seamless round steel pipes were used for all components in this study. For better mechanical performance and installation reliability, 20 mm thick end plates were attached to both ends of the circular hollow section by welding. Stiffening ribs were welded at 45-degree intervals at both ends of the component to enhance its stiffness and prevent end failure during the loading process. It is worth noting that all stiffeners are made of the same steel as the component. The dimensions and parameters of the component are detailed in Fig. 2.

2.3. Material tests

The material properties of the CHS component were obtained through tensile testing. The test components were made from seamless round steel pipes with four different thicknesses: 8.00 mm, 6.00 mm, 4.00 mm, and 3.50 mm. Therefore, 12 samples with varying thicknesses were cut along the rolling direction from the same batch of plates as the loaded components. The tensile tests were executed according to GB/T 228.1 [21]. The length of the 8.00 mm components was 250 mm, while the lengths of the 6.00 mm, 4.00 mm, and 3.50 mm components were 240 mm. The experiments were conducted using an MTS testing machine, and deformation was recorded with a 50 mm extensometer. The loading rate was initially set to 0.5 mm/min until the strain reached 2.5%. After this, the loading rate was increased to 2 mm/min until the components fractured. Table 2 summarizes the average results of the material performance parameters, where t represents the thickness of the component, f_y is the yield strength, f_u is the ultimate tensile strength, E is the Young's modulus and e is the elongation rate.

Table 2
Material properties

Grade	t(mm)	fy (MPa)	fu (MPa)	E (GPa)	e
355	8	371.04	546.29	192.85	31
355	6	361.68	547.61	229.23	31
355	4	375.31	573.60	234.21	25
355	3.5	377.01	567.08	227.212	29

2.4. Geometric imperfection measurement

Initial geometric defects are commonly present in round steel pipes during the manufacturing process, which can influence the test results. Therefore, this study employed laser scanning technology to measure the initial geometric defects of the components [22]. Prior to scanning, marker spots were applied to the component surface. A handheld laser scanner was used to measure the 3D profile of the outer surface, recording point clouds at different scanning positions. The scanning data was then fed back to a computer to create a real-time model of the point cloud, with a measurement accuracy of 0.01 mm, as shown in Fig. 3.

The measurement results of each sample indicate that the defect amplitude varies slightly for each cross-section and height. Select five different cross-sections 150mm above the stiffening ribs at the bottom of the sample, with an interval of 150mm between each cross-section for analysis, and select 200 data points for each cross-section to form the curve shown in Fig. 4. The outer surface contour distribution of cross-sections A-C-219 × 8, A-C-219 × 6, A-C-219 × 4, and A-C-219 × 3.5 is shown in Fig. 5. The consistent results indicate that each cross-section has two radius peaks, which means the cross-section is approximately elliptical. Local defects in each component are strictly controlled within 1/200 of the diameter, meeting the requirements of GB 50205-2020 [23].

Fig. 3 Laser scanner test

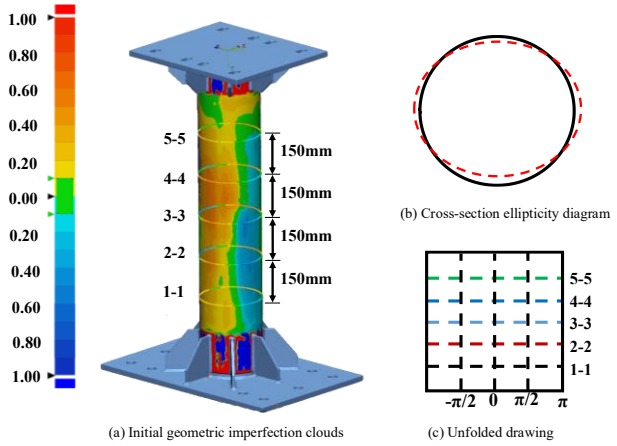

(a) Initial geometric imperfection clouds (b) Cross-section ellipticity diagram (c) Unfolded drawing

Fig. 4 Component imperfection distribution

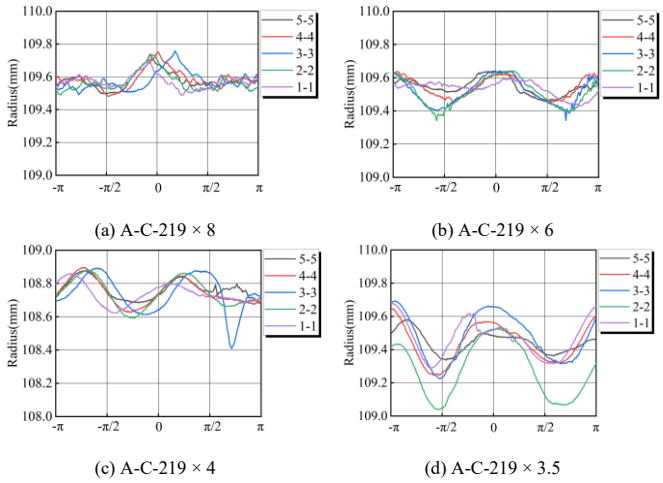

(a) A-C-219 × 8 (b) A-C-219 × 6

(c) A-C-219 × 4 (d) A-C-219 × 3.5

Fig. 5 Distribution of outer-surface curves of components

2.5. Test setup

The experimental loading device is shown in Fig. 6, which is used for quasi-static testing of steel components. The bottom of the component is fixed to the base using M30 high-strength bolts, while the top is connected to the loading beam via a connector and pin shaft. Additionally, the experimental device is equipped with a four-bar linkage to constrain the outer surface of the component, ensuring that there is no out of plane displacement during the loading process. During the experiment, a 1000kN hydraulic jack was first used at the top to apply axial force. After maintaining stability, the MTS electro-hydraulic servo actuator (maximum load of 500kN) was used to drive the distribution beam to apply horizontal load until the experiment was stopped.

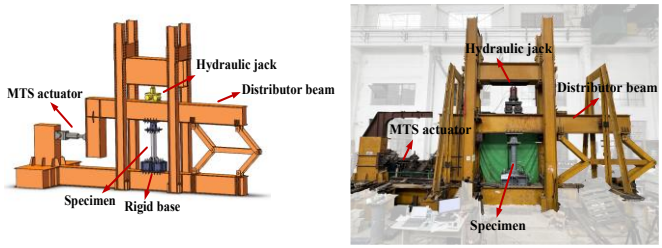

(a) Schematic diagram (b) Photo of the site layout

Fig. 6 Test setup

Several sensors were employed in the experimental setup. The constant axial force was applied and monitored using a hydraulic jack, while the lateral force was measured by an MTS hydraulic actuator. As shown in Fig. 7(a), nine linear variable displacement sensors were installed to monitor the displacement response throughout the testing period. D1 and D2 were used to measure the horizontal displacement within the top plane of the column; D3 monitored the horizontal displacement outside the top plane of the column; D4 measured the horizontal displacement within the column plane; D5 monitored the horizontal displacement outside the column plane; D6 measured the horizontal slip within the base plane of the column; D7 monitored the horizontal slip outside the column base plane; and D8 and D9 were used to monitor the rotation of the column base.

As shown in Fig. 7(b)(c), a series of strain gauges were installed, and Digital Image Correlation (DIC) non-contact measurement technology was used to track the deformation response during the test. This method was primarily employed to determine the bottom bulge and the height of the equivalent plastic zone of the column.

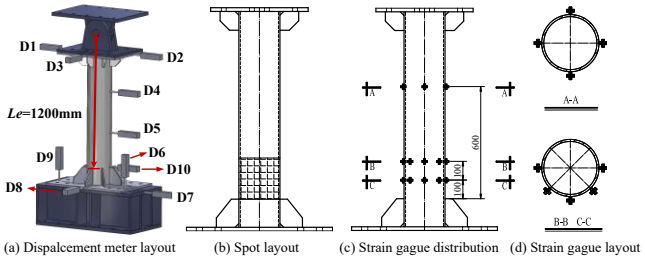

(a) Dispalcement meter layout (b) Spot layout (c) Strain gague distribution (d) Strain gague layout

Fig. 7 Component measurement programme

2.6. Loading protocol

The cyclic tests followed the non-uniform cyclic loading protocol outlined in ANSI/AISC 341 [24], using a quasi-static drift angle θ control. As illustrated in Fig. 9, the drift angle was calculated as $\theta = \Delta/L_e$, where Δ represents the horizontal displacement at the top of the component, and L_e denotes its effective length. The drift angle loading sequence included 0.375%, 0.50%, 0.75%, 1.0%, 1.5%, and 2.0%. Specifically, drift angles of 0.375%, 0.50%, and 0.75% were applied for six cycles each, while the 1.0% drift angle was applied for four cycles. For the remaining drift levels, two cycles were applied per level, with the drift angle increasing by 1.0% every two cycles thereafter, as illustrated in Fig. 10. To manage the overall test duration, different displacement rates were adopted: a rate of 0.2 mm/s was used when Δ equaled 0.00375 L_e; for displacements below 0.03 L_e, a rate of 0.5 mm/s was applied; and for values exceeding 0.03 L_e, the rate was increased to 1 mm/s. Both monotonic and cyclic loading processes continued until either distinct local buckling developed at the specimen's base or a sudden decline was detected in the load-displacement response.

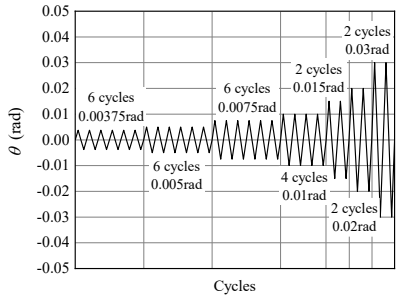

Fig. 8 Cyclic loading protocol

3. Test results

3.1. Experimental phenomena

The deformation development and failure phenomena of each component are similar. Six steel circular hollow sections undergo three stages of elasticity, elastoplasticity and failure in constant axial compression and low-cycle repeated tests. The final failure mode is shown in Fig. 9. Taking the typical component A-C-219×4-0.2 as an example, the test process and phenomenon are described in detail.

In the early stage of loading, before the drift angle reached 0.015, the transverse and longitudinal strain values of the circular hollow section were small, and the component exhibited no apparent phenomena (Fig. 10a). When the drift angle reached 0.015, slight bulging appeared on the right side of the component (Fig. 10b). As the drift angle increased to 0.02, buckling in the right compression zone became more pronounced. When the drift angle reached 0.03, annular deformation occurred, and the steel circular hollow section experienced severe buckling. When the drift angle reached 0.04, the circular hollow section deformed excessively, and the accumulated residual deformation led to a 'lantern'-shaped buckling. The component underwent significant plastic deformation, its load-bearing capacity was greatly reduced, and the test was completed.

Fig. 9 Final failure mode of the component

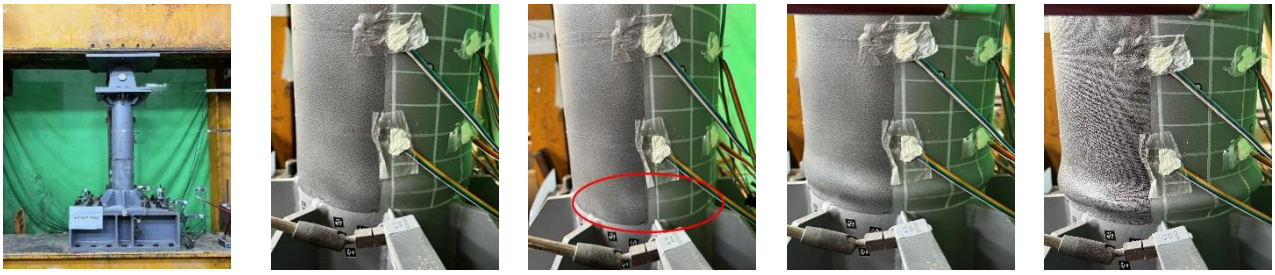

(a) Initial stage of test (b) $\theta = 0.015$ (c) $\theta = 0.02$ (d) $\theta = 0.03$ (e) $\theta = 0.04$

Fig. 10 Process of component failure

(a) A-C-219×8-0.2 (b) A-C-219×8-0.4 (c) A-C-219×8-0.6

(d) A-C-219×6-0.2 (e) A-C-219×4-0.2 (f) A-C-219×3.5-0.2

Fig. 11 Failure mode of test piece

The final failure mode of each component was shown in Fig. 11. Each component behaved similarly to the typical specimen A-C-219×4-0.2. Local buckling occurred at the end of the component, forming a ring-like buckling of the circular hollow section and resulting in large plastic deformation. However, components A-C-219×8-0.2 and A-C-219×8-0.4 exhibited tearing and cracking of the circular hollow section near the stiffener. Since the stiffener was directly welded onto the circular hollow section, the component was relatively weak at the welding location. In the middle and late stages of loading, the upper portion of the steel circular hollow section near the stiffener tore or cracked, leading to the termination of the test. However, the failure of the components occurred after reaching the ultimate bearing capacity, and was not caused by a decrease in bearing capacity due to weld crack.

3.2. Hysteretic responses

The hysteretic behavior of a structural component under cyclic loading reflects its deformation characteristics during repeated loading, which is typically represented by the moment–drift angle curve. The total bending moment M comprises a first-order moment M_1, induced by the applied lateral force, and a second-order moment M_2, resulting from the axial load acting on the lateral displacement at the column top. The moment-rotation hysteresis curve of the circular steel circular hollow section component under cyclic loading is shown in Fig. 12, where the abscissa is the drift angle of the loading part of the component, and the ordinate is the bending moment applied to the component. By comparing the hysteresis curves and characteristics of each component, the following conclusions can be drawn : 1) The hysteresis curves of each component show a relatively full spindle shape and have good energy dissipation capacity. 2) Each component experiences elastic stage, yield stage and failure stage. 3) After the peak load, the bearing capacity of each component did not decrease sharply, showing the characteristics of ductile failure. 4) With the increase of axial compression ratio, the hysteresis curve area of the component decreases and the energy dissipation capacity decreases. 5) Under the coaxial pressure ratio, the drift angle of local buckling of the component with cross-section grade S1 is larger than that of the component with cross-section grade S2, and presents a certain rule. Therefore, with the increase of the diameter-thickness ratio, the local buckling of the component occurs earlier.

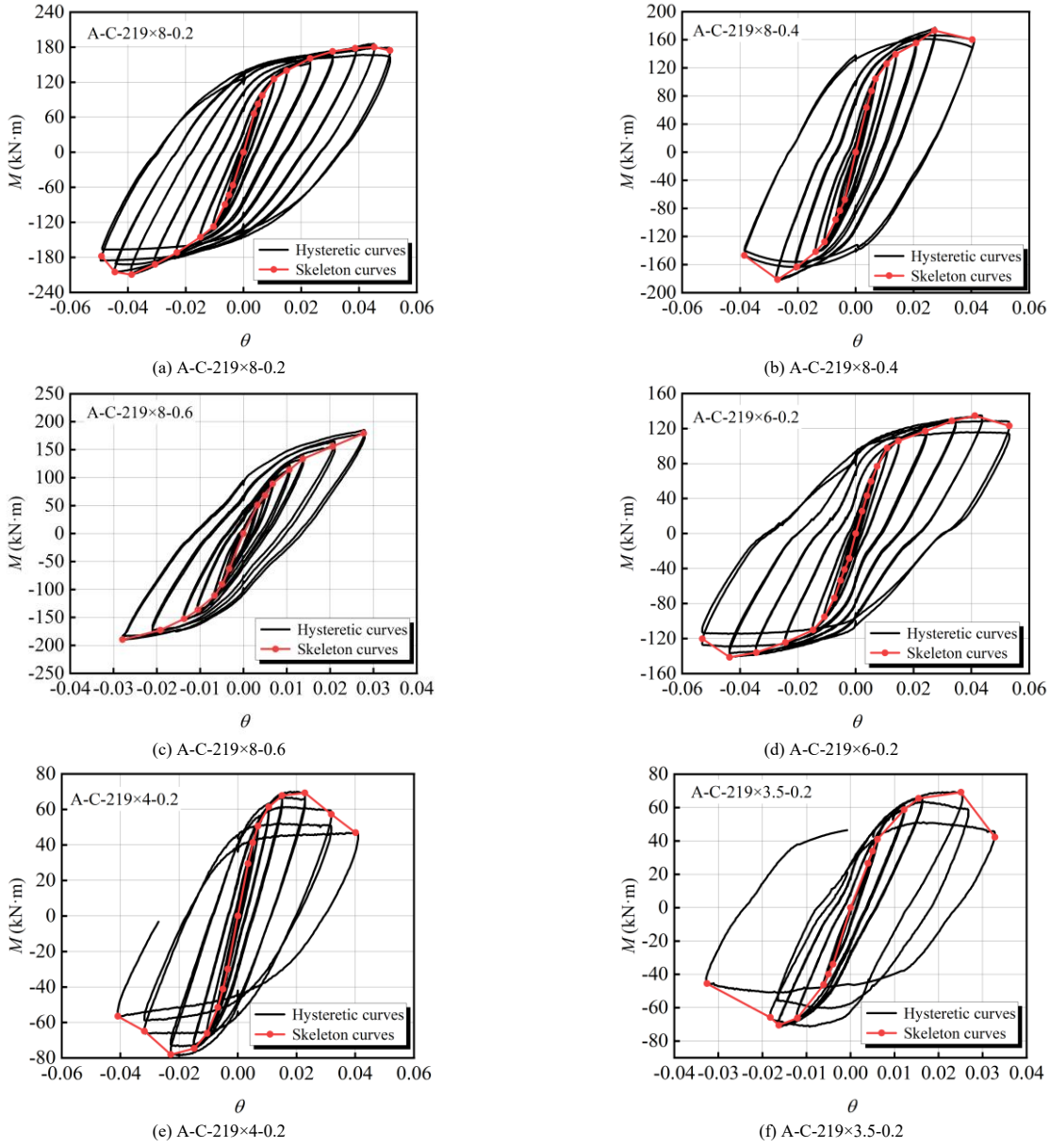

(a) A-C-219×8-0.2 (b) A-C-219×8-0.4

(c) A-C-219×8-0.6 (d) A-C-219×6-0.2

(e) A-C-219×4-0.2 (f) A-C-219×3.5-0.2

Fig. 12 Hysteretic loops and skeleton curves of components

3.2.1. Measurement of plastic zone length

The distance from the peak or trough of the member's buckling waveform to the root of the member is defined as half of the equivalent plastic zone length. The Digital Image Correlation (DIC) technique can accurately measure the component plastic zone length L_h [25]. According to the theory of elasticity [26], the flexural half-wave length of a circular pipe section is the distance from the crest to the trough of the wave, which is calculated by the formula (1), which can be approximated as half of the equivalent plastic zone length of a circular pipe section, i.e., $L_h/2$.

DIC technology can record the deformation development of the component in real time, and the corresponding local buckling length in the limit state is taken as the equivalent plastic zone length L_h of the component. Taking the component A-C-219×4-0.2 as an example, the plastic zone length L_h is accurately measured in the data processing software, as shown in Fig. 15. The measured value of the component and the approximate value calculated by Eq. (1) are listed in Table 3. It can be seen that the calculated value of the formula is close to the measured value.

The Digital Image Correlation (DIC) technique enables real-time recording of the deformation evolution of test components. Taking component A-C-219×4-0.2 as an example, L_h was accurately measured using the data processing software as illustrated in Fig. 15. The measured values of the components, along with the approximate values calculated using Eq. (1), are listed in Table 3. It can be observed that the calculated results show good agreement with the experimental measurements.

$$L_{cr}=1.72\sqrt{(R-\frac{t}{2})t} \quad (1)$$

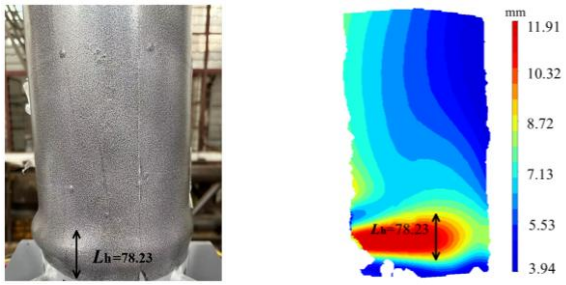

Fig. 13 Measurement of L_h for test component A-C-219×4-0.2

Table 3
Equivalent plastic zone length

Component number	Measured value	Formula value	Error
A-C-219×8-0.2	110.33	99.92	9.41%
A-C-219×8-0.4	110.25	99.92	9.32%
A-C-219×8-0.6	110.36	99.92	9.4%
A-C-219×6-0.2	85.33	88.34	3.56%
A-C-219×4-0.2	78.23	71.32	8.85%
A-C-219×3.5-0.2	65.62	66.80	1.83%

4. Definition of strain ductility coefficient

4.1. Equivalent plastic zone

The experiment shows that the region near the maximum bending moment of the steel member with circular pipe section is also the concentrated area of plastic and local buckling deformation of the member. Based on the stress characteristics of cantilever members, the area of local instability is defined as the 'equivalent plastic zone ' [27], and the following assumptions are made when defining the equivalent plastic energy consumption area [28]:

(1) The curvature is assumed to be constant throughout the equivalent plastic zone and the bending moment is taken as the maximum value occurring within this zone;

(2) Ignore the shear deformation in the equivalent plastic zone of the flexural members [29];

(3) The flexural member is divided into elastic section and equivalent plastic zone. The local buckling of the members occurs in the equivalent plastic zone, and the elastic segment remains elastic throughout the loading process;

(4) No overall bending torsional instability of members

4.2. Curvature of equivalent plastic zone

According to the assumptions (3) and (4) in Section 4.1, the total horizontal displacement of the cantilever member Δ is composed of the horizontal displacement of the elastic section Δ_{es} and the deformation of the equivalent plastic zone Δ_h. As shown in Fig. 14, the deformation of the equivalent plastic zone consists of the deflection deformation Δ_{h1}, the rotational deformation of equivalent plastic zone Δ_{h2} and the shear deformation of the equivalent plastic zone Δ_{h3}. Since the shear deformation of the equivalent plastic zone is small, the shear deformation of the equivalent plastic zone Δ_{h3} is ignored according to assumption (2) in section 4.1.

$$\Delta = \Delta_{es}+\Delta_{h1}+\Delta_{h2}+\Delta_{h3} \quad (2)$$

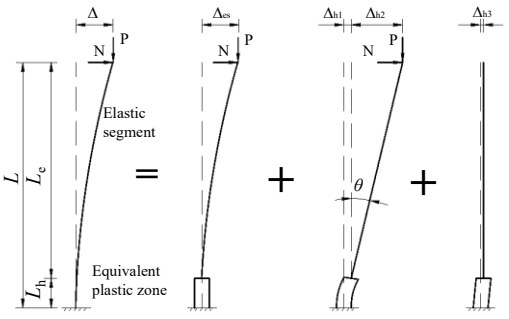

Fig. 14 Decomposition diagram of component deformation

The horizontal displacement of the elastic segment is calculated in Eq. (3). The notation used in this equation is as follows: Δ_f and Δ_s represent the elastic bending deformation and shear deformation of the elastic segment of the cantilever component; F is the lateral load at the top of the cantilever component; E and G are the elastic modulus and shear modulus of the steel material, respectively; I is the moment of inertia of the cross-section of the cantilever component; A is the cross-sectional area of the cantilever component; L_e is the length of the elastic segment; κ is the coefficient of shear stress non-uniformity, with a typical value of 10/9 for circular hollow section cross-sections [30].

$$\Delta_{es} = \Delta_f + \Delta_s = \frac{FL_e^3}{3EI} + \frac{FL_e}{\kappa GA} \quad (3)$$

Based on assumption (1) in section 4.1, it is assumed that the curvature of the section is uniform in the equivalent plastic zone. Therefore, the average curvature of the equivalent plastic zone is expressed by Eq. (4), where R is the radius of curvature of the plastic energy plastic zone.

$$\varphi = \frac{1}{R} \quad (4)$$

According to the schematic diagram, the calculation formula of bending deformation in the equivalent plastic zone of the member is given by Eq. (5), where θ is the section angle at the end of the plastic zone. When θ is small, Eq. (5) can be simplified as Eq. (6). In Eq. (6), L_h is the length of equivalent plastic zone.

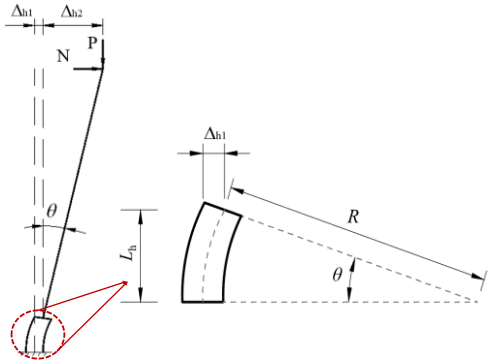

Fig. 15 Calculation diagram

$$\Delta_{h1} = R(1-\cos\theta) = 2R\sin^2\frac{\theta}{2} \quad (5)$$

$$\Delta_{h1} \approx 2R\left(\frac{\theta}{2}\right)^2 = \frac{R\theta^2}{2} = \frac{L_h^2}{2}\varphi \quad (6)$$

The deformation Δ_{h2} induced by the rotation of the equivalent plastic energy is given by Eq. (7). By substituting Δ_{h1} and Δ_{h2} into Eq. (1), the formula for the equivalent plastic zone curvature is derived as Eq. (8).

$$\Delta_{h2} = \theta L_e = \varphi L_h L_e \quad (7)$$

$$\varphi = \frac{\Delta-\Delta_{es}}{L_eL_h + L_h^2/2} = \frac{\Delta-\Delta_{es}}{(L-L_h/2)L_h} \quad (8)$$

Where Δ_{es} is the horizontal displacement of the elastic section, which can be directly calculated based on elastic theory, and Δ is the horizontal displacement at the loading point of the member, which can be directly extracted from the calculation results of the cantilever member. Therefore, the average curvature of the equivalent plastic zone can be determined using the equivalent plastic length L_h, the total horizontal displacement of the member Δ, and the horizontal displacement of the elastic section Δ_{es}.

4.3. Equivalent strain

According to the assumption that the section curvature in the equivalent plastic zone is equal, the strain in the equivalent plastic zone can be calculated by Eq. (9).

$$\varepsilon_{max} = \varepsilon_0 + \varepsilon_f = n\varepsilon_y + \frac{\varphi h}{2} \quad (9)$$

The notation used in this equation is as follows: ε_0 is the strain caused by axial pressure, ε_f is the section edge strain caused by bending, n is the axial compression ratio, ε_y is the yield strain, and h is the section height. Therefore, the effect of the ultimate deformation of the member is changed into Eq. (10).

$$\varepsilon_u = n\varepsilon_y + \frac{\varphi_u h}{2} \quad (10)$$

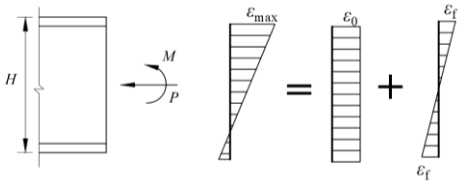

Fig. 16 Equivalent strain in the plastic zone

4.4. Strain ductility coefficient

In reference [18], the ratio of the strain corresponding to the reduction of the ultimate load of the member to 85 % to the strain corresponding to the yield of the section edge of the member is defined as the ' strain ductility coefficient ' [31]. The strain ductility coefficient can directly represent the plastic deformation development ability of the component. In the equation of strain ductility coefficient (11), ε_y is the strain corresponding to the yield of the section edge of the member and ε_u is the ultimate strain of the section. In this paper, ε_u is defined as the strain in the plastic zone corresponding to the 15% reduction of the peak load [32].Where Δ_{es} denotes the horizontal displacement of the elastic section and it can be calculated using equation(2); where Δ is obtained from loading tests; L_h can be approximated by Eq. (1); L denotes the member length and h represents the diameter of the circular cross-section.

$$\mu_\varepsilon = \frac{\varepsilon_u - \varepsilon_y}{\varepsilon_y} \quad (11)$$

$$\mu_\varepsilon = \frac{2(n-1)\varepsilon_y + \frac{(\Delta - \Delta_{es})h}{(L - L_h/2)L_h}}{\varepsilon_y} \quad (12)$$

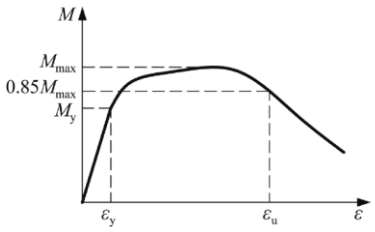

Fig. 17 Ultimate deformation of components

5. Numerical modeling

5.1. Establishment of finite element models

The finite element model of the component was established by ABAQUS. The ' S4R ' shell element had been widely used to simulate the cross-section members under various loading conditions. Therefore, the S4R shell element was used for the steel circular hollow section components and stiffeners in this paper. A mesh sensitivity analysis was first conducted with mesh sizes of 15 mm, 10 mm, and 5 mm. The results indicate that: (i) the 15 mm mesh significantly improved computational efficiency but led to reduced accuracy, with deviations exceeding 3% compared to the 10 mm mesh; (ii) the 5 mm mesh yielded results that were in close agreement with those of the 10 mm mesh, with average discrepancies within 1%. Considering both computational efficiency and accuracy, a mesh size of 10 mm was ultimately selected for subsequent analyses [33]. The bottom and top of the model were coupled to points RP2 and RP1 respectively, which had been successfully applied in Ref. [34]. Fixed boundary conditions were applied at the bottom of the model, while the top was constrained against out-of-plane displacement and rotation. The vertical pressure and reciprocating horizontal displacement were applied at the centroid point RP1. The loading system was described in the previous chapter. The same axial pressure as the test is used in the calculation and analysis.

The steel constitutive model used in the parametric analysis adopted a nonlinear combined hardening material model. The key parameters were taken from Ref. [35], as shown in Table 2. For the verification model, the elastic modulus and yield strength of the steel were determined based on the test results in Table 4.The first-order buckling mode obtained from the eigenvalue analysis was applied to the model as the initial geometric imperfection. For the local initial geometric defects of the verification model, the measured values of the 3D-scanned components were used. For the model of parametric analysis, the maximum value of local initial geometric defects was taken as 1/10 of the wall thickness [22].

Table 4
Basic parameters of the cyclic material model adopted in the FE modelling

Grade	$\sigma_{\|0}$ (MPa)	E (MPa)	C_1 (MPa)	γ_1	C_2 (MPa)	γ_2	C_3 (MPa)	γ_3	C_4 (MPa)	γ_4
Q355	355	206000	7993	175	6773	116	2136	34	1450	29

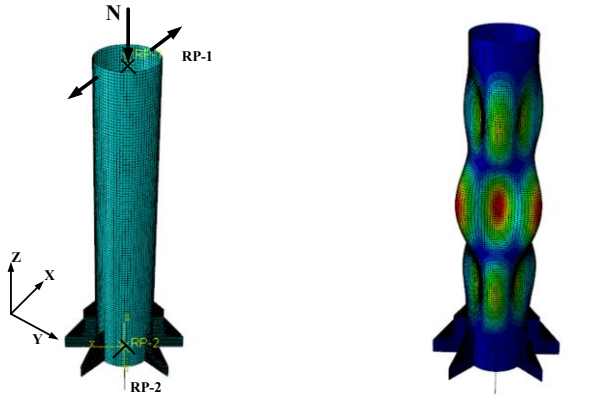

(a) FE model (b) Local buckling mode

Fig.18 Finite element model

5.2. Finite element model validation

The FE model was verified based on the experimental results of 6 components. Fig. 19 shows the failure mode of the component A-C-219×6-0.2 from both the finite element model and the test components, as well as the deformation corresponding to the plastic zone length at the same time. It was observed that the finite element model accurately simulated the local buckling at the bottom of the component and other components exhibited similar failure phenomena which were consistent with the test results. Fig. 20 shows the comparison of the bending-drift angle curve and the skeleton curve of the six component tests and the FE model. The results indicated that the shapes of the skeleton curve of the ultimate bending moment of the test and the finite element simulations were basically the same and matched well. In general, the established finite element model accurately reproduced the mechanical behavior of the circular steel circular hollow sections under cyclic loading and was suitable for subsequent parametric analysis.

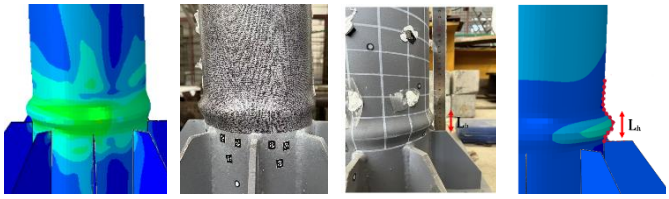

(a) FE failure mode (b) Experimental failure mode (c) Component plastic zone length (d) FE plastic zone length

Fig. 19 Comparison between finite element method and experiment

6. Analysis of parametric analysis results

6.1. Parametric study

The parameter study of the verified finite element model was conducted to expand the database, considering the diameter-thickness ratio, axial compression ratio, and loading system of compression-bending members as the main factors. For the model used for parameter analysis, the elastic modulus of steel is E = 206 kN / mm, the yield strength of steel is f_y = 355 MPa, and the Poisson 's ratio is v = 0.3. The diameter-thickness ratio of steel members with circular hollow section ranges from 20 to 66, with a total of 8 different groups of values designed. The axial compression ratios are 0.2, 0.3, 0.4, 0.5, and 0.6, with 5 different groups of values. The materials considered are primarily Q355. For modeling convenience, the length of the members is set to 1200 mm, with boundary conditions and the loading system identical to those of the previously verified finite element model.

6.2. Analysis of factors influencing the strain ductility coefficient

The parametric analysis provided the basis for calculating key limit state parameters, including total displacement and plastic zone length. The strain ductility coefficient of each component is then calculated according to the definition of the strain ductility coefficient, and the effects of different factors are analysed.

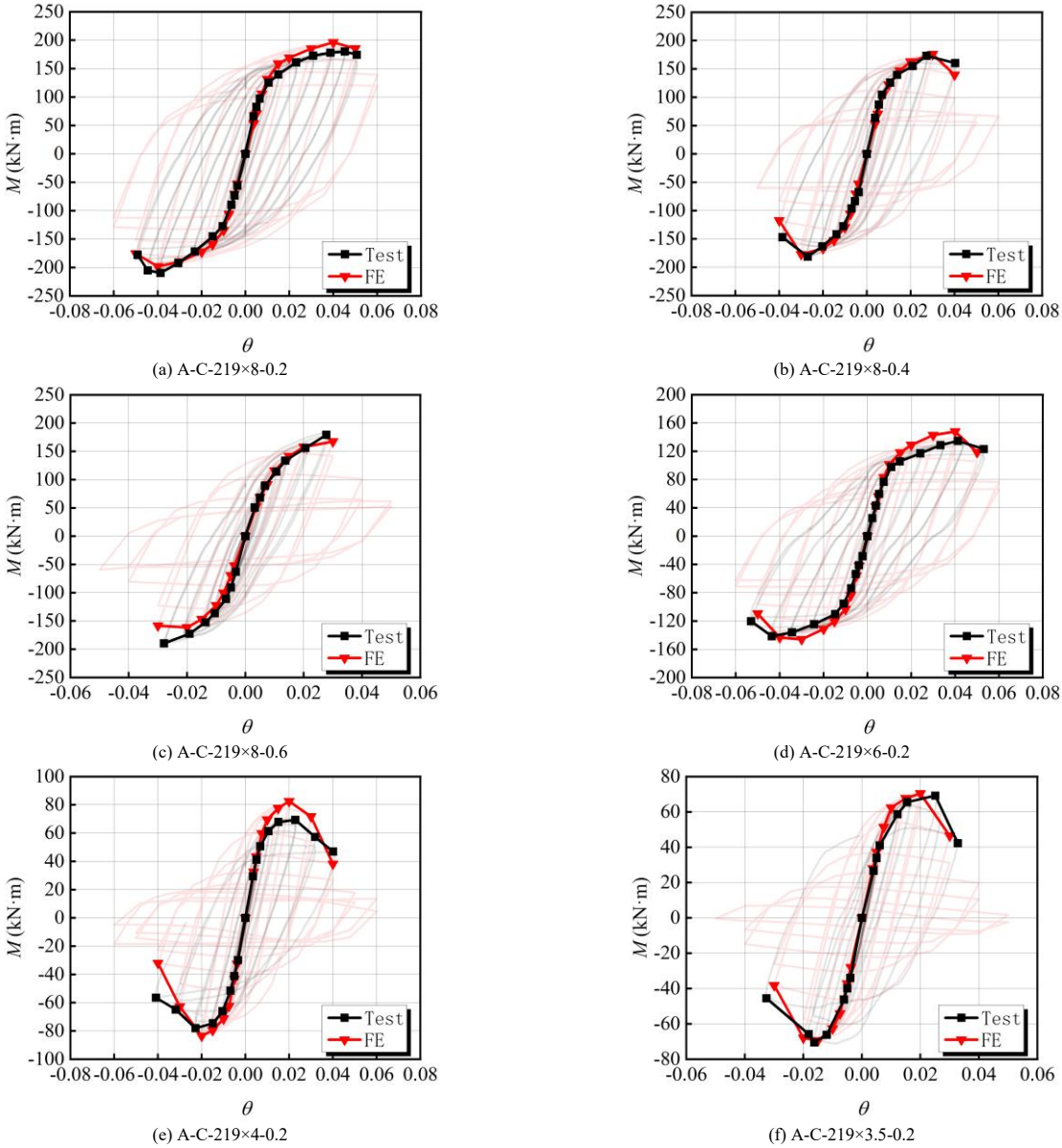

(a) A-C-219×8-0.2 (b) A-C-219×8-0.4

(c) A-C-219×8-0.6 (d) A-C-219×6-0.2

(e) A-C-219×4-0.2 (f) A-C-219×3.5-0.2

Fig. 20 Comparison of hysteresis curve and skeleton curve between experimental and finite element simulation

6.2.1. Impact of loading protocol

The deformation capacity of circular section members under two loading systems was investigated using finite element simulations. These two loading protocols are symmetrical cyclic loading protocol and collapse-consistent loading protocol. The symmetrically cyclic loading protocol, which corresponds to the experimental procedure described above, is a commonly used method in the seismic performance evaluation of structural components. The collapse-consistent loading protocol was proposed by LIGNOS in 2014 [36]. The collapse-consistent loading protocol inserts a large one-way push-over displacement between several elastic-plastic loading cycles, which is considered to be more in line with the characteristics of seismic action.

The bending moment-displacement curves of circular section steel members with axial compression ratio of 0.2 section under collapse-consistent loading protocol and symmetrically cyclic loading protocol are compared, as shown in Fig. 21. The symmetrically cyclic loading protocol is usually more unfavorable than the earthquake action, and the collapse-consistent loading protocol can be regarded as a typical seismic wave as a disordered loading system. Table 5 is the comparison of strain ductility coefficient of the components under the two loading protocols. The analysis results indicate that:(1) The strain ductility coefficient under the collapse-consistent loading protocol are consistently higher than those obtained under symmetrically cyclic loading protocol;(2) The rate of strength degradation after the component reaches its peak load under the collapse-consistent loading protocol is significantly lower than that under symmetrically cyclic loading protocol;(3) For components with the same diameter-to-thickness ratio, a higher axial compression ratio leads to a larger difference in strain ductility coefficient between the two loading protocols. Since structural components were more vulnerable under symmetric cyclic loading, only symmetric cyclic loading was adopted in the subsequent parametric analyses.

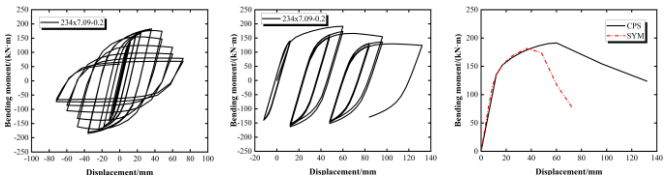

(a) Symmetrically cyclic loading protocol n-0.2 (a) Collapse-consistent loading protocol n-0.2 (c) Skeleton curve comparison n-0.2

Fig. 21 Comparison of bending moment-displacement curves under different loading protocols

6.2.2. Effect of diameter-thickness ratio

Fig. 21 shows the distribution of strain ductility coefficients of models with different diameter-to-thickness ratios under horizontal reciprocating loads. It shows that the diameter-to-thickness ratio of the circular cross-section steel members has a significant effect on the strain ductility coefficient. Generally, as the diameter-to-thickness ratio increases, the strain ductility coefficient of the model decreases.

Table 5

Comparison of strain ductility coefficient of components under different loading protocols

Component number	Collapse-consistent loading protocol	Symmetrically cyclic loading protocol	Ratio
234x7.09-0.2	48.13	25.45	1.89
234x7.09-0.4	37.4	18.08	2.06
234x7.09-0.6	32.26	9.85	3.27
234x5.08-0.2	35.79	22.4	1.59
234x5.08-0.4	23.54	13.41	1.75
234x5.08-0.6	17.29	8.4	2.05
234x3.96-0.2	25.92	17.87	1.45
234x3.96-0.4	17.16	10.35	1.65
234x3.96-0.6	10.37	5.62	1.84
234x3.54-0.2	21.72	17.2	1.26
234x3.54-0.4	14.74	10.61	1.38
234x3.54-0.6	7.46	5.23	1.42

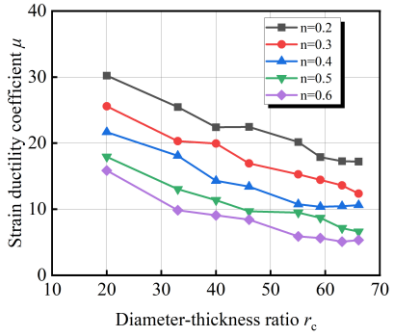

Fig. 22 Influence of diameter to thickness ratio

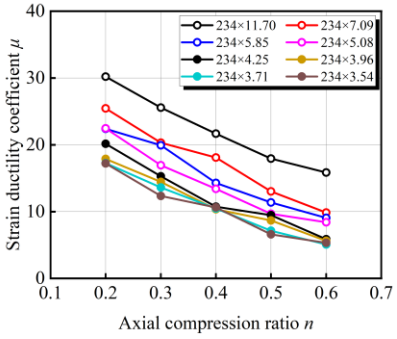

Fig. 23 Effect of axial compression ratio

6.2.3. Effect of axial compression ratio

The variation of the strain ductility coefficient of circular cross-section steel members under horizontal cyclic loading with axial compression ratios of 0.2, 0.3, 0.4, 0.5, and 0.6 is shown in the Fig. 22. As shown in Fig. 22, the strain ductility coefficient of the compression-bending circular cross-section steel members decreases as the axial compression ratio increases.

6.2.4. Empirical formula for strain ductility factor

The analysis of the results indicates that for compression-bending members, both the diameter-to-thickness ratio and the axial compression ratio of the component section are important factors affecting the strain ductility coefficient of the compression-bending steel members. Among them, the axial compression ratio is negatively correlated with the strain ductility coefficient and the diameter-thickness ratio of the member is inversely correlated with the strain ductility coefficient. Therefore, the functional relationship of the strain ductility coefficient of steel members with circular hollow section is shown in the following equation (13).

$$\mu_{fc} = \frac{a}{r_c} + b r_c^{c} (1 - kn)^{d} \quad (13)$$

Where r_c (r_c=D/t)is the diameter-to-thickness ratio, n is the axial pressure ratio, and a, b, c, and d are constants to be determined. Based on the regression analysis of the parameter analysis results in this study, the values of the aforementioned constants can be determined. The empirical formula for calculating the strain ductility coefficient of Q355 members is given as follows:

$$\mu_{fc} = \frac{300}{r_c} + 50 r_c^{-0.2} (1 - 1.4n)^{1.6} \quad (14)$$

Fig. 24 shows the comparison between the calculated and experimental values of the test members obtained according to the strain ductility coefficient empirical formula. The experimental value is the result of the test of six specimens according to the formula (14) in section 4.3 ; the calculated value is the result of fitting according to formula 14. It can be seen that the calculated values have a high degree of agreement with the tested and simulated values. Therefore, the strain ductility coefficient formula can be reliably used to predict the strain-based deformation capacity of circular cross-section steel members.

Since the 219×3.5 circular hollow section was fabricated from 219×6 circular circular hollow section, manufacturing deviations resulted in an actual wall thickness smaller than the design thickness. Consequently, the obtained strain ductility coefficients was relatively low, leading to a higher relative error.

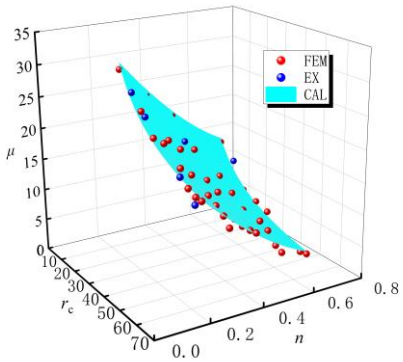

Fig. 24 Comparison of calculated strain ductility coefficient values with simulated and experimental values

Table 6

Comparison between experimental and calculated values of strain ductility coefficient

Component number	Experimental value	Calculated value	Error
A-C-219×8-0.2	27.57	26.20	4.96%
A-C-219×8-0.4	18.55	17.89	3.55%
A-C-219×8-0.6	13.77	12.33	10.45%
A-C-219×6-0.2	24.90	22.98	7.71%
A-C-219×4-0.2	18.84	18.75	0.47%
A-C-219×3.5-0.2	16.08	17.72	10.19%

7. Conclusion

This paper proposes a strain ductility coefficient based on the equivalent plastic zone to evaluate the deformation of circular hollow section steel components. The effects of different parameters on the strain ductility coefficient are investigated by conducting low circumferential reciprocating tests and finite element analysis. Based on the research results, this paper proposes an empirical formula for the strain ductility coefficient. The main conclusions are as follows:

(1) For circular hollow section steel members with different diameter-to-thickness ratios, local buckling occurs at the bottom under cyclic loading. According to the principle of equal total deformation of members, the strain-based ductility coefficient is proposed to provide a theoretical basis for evaluating the deformation capacity of members.

(2) According to the test and finite element result, the ultimate strain and strain ductility coefficient of the circular cross-section steel member decreases with the increase of the member diameter-to-thickness ratio and axial pressure ratio.

(3) Based on the finite element and experimental results, this paper proposes a suggested empirical formula for the strain ductility coefficient. The empirical formula is accurate and effective, as demonstrated by comparisons with experimental data and finite element (FE) results, with a maximum error not exceeding 15%.

It is important to note that the experimental program in this study was conducted using steel with a nominal yield strength of 355 MPa. Moreover, the proposed Equation (14) does not account for the influence of different steel strength grades. As the strength of steel increases, a reduction in ductility is typically observed. To enhance the applicability and generalization of the proposed equation and conclusions, further investigations are required to incorporate the effect of steel strength and develop appropriate modifications. In addition, the present study is focused on circular steel members governed by a local buckling failure mode. Other potential failure mechanisms, such as shear failure, global instability, and fatigue damage, involve distinct deformation characteristics and failure mechanisms, and they are not within the scope of the conclusions of this study.

References

[1] M.J. Priestley, Performance based seismic design. In: 12th World Conferences on Earthquake Engineering, 2000, pp. 2831-2852.

[2] M. Elchalakani, X.L. Zhao, R.H. Grzebieta, Plastic mechanism analysis of circular tubes under pure bending, International Journal of Mechanical Sciences 2002;44:1117–1143.

[3] Dalal Sejal P, Vasanwala, Desai A K, Performance based seismic design of structure: A review. International journal of civil and structural engineering 2011;1:795-803.

[4] SEAOC. A framework for performance-based engineering: Vision 2000. California: Structural Engineering Association of California, 1995.

[5] FEMA-273 Nehrp guidelines for the seismic rehabilitation of buildings. Washnigton, DC: Federal Emergency Management Agency; 1997.

[6] TBI Guidelines Working Group. Guidelines for performance-based seismic design of tall buildings. California, peer report: Pacific Earthquake Engineering Research Center; 2010.

[7] FEMA 356. FEMA-356 Prestandard and Commentary for the Seismic Rehabilitation of Buildings. Washnigton, DC: Federal Emergency Management Agency; 2000.

[8] ASCE 41-13. ASCE41–13 Seismic Evaluation and Retrofit of Existing Buildings. Reston, VA: American Society of Civil Engineers; 2014.

[9] ASCE 41-17. Seismic Evaluation and Retrofit of Existing Buildings. Reston, Virginia: American Society of Civil Engineers, Ed.; American Society of Civil Engineers; 2017.

[10] GB 50017—2017. Standard for design of steel structures. Beijing: China Architecture & Building Press; 2018 [in Chinese].

[11] GB 50011-2010. Code for seismic design of buildings. Beijing: China Architecture & Building Press; 2018 [in Chinese].

[12] Fan Zhong, Chai huijuan, Chen Yuchen, et al. Deformation Performance of Steel Pipe Columns. Journal of Tianjin University(Science and Technology) 2021;54:133-143 [in Chinese].

[13] X. Meng, L. Gardner, Stability and design of normal and high strength steel CHS beam-columns, Engineering Structures 251 (2021) 113361.

[14] B. Zheng, Z. Chen, J. Yao, H. Fu, L. Wang, G. Shu, Tests on seismic performance of hot-rolled stainless steel circular hollow section beam-columns, Structures 74 (2025) 108611.

[15] J. Xing, Y. Tian, Q. Yang, Y. Huang, G. Xu, Hysteretic performance of CHS steel members under cyclically fluctuating axial loads and lateral displacement, Engineering Structures 199 (2019) 109602.

[16] Wang kaifei, Shaofangfang, et al. Research on hysteretic behavior of steel circular-tube members under constant compression and cyclic bending. Journal of Building Structures 2010;31:35-38 [in Chinese].

[17] M. Elchalakani, X.-L. Zhao, R. Grzebieta, Cyclic bending tests to determine fully ductile section slenderness limits for Cold-Formed circular hollow sections, Journal of Structural Engineering 130 (2004) 1001–1010.

[18] Z. Guo, J. Yang, Z. Li, Y. Chen, Experimental investigation on hysteretic behavior of circular hollow steel tubular columns after lateral impacts, Engineering Structures 232 (2021) 111861.

[19] C. Fang, F. Wang, C. Wang, Y. Zheng, Cyclic behavior of oval hollow section (OHS) beam-columns, Thin-Walled Structures 161 (2021) 107430.

[20] J. Zhang, G.-P. Shu, D. Yang, L.-L. Yang, Estimation of deformation capacity of steel beam-columns based on strain ductility coefficient, Structures 46 (2022) 1517–1531.

[21] GB/T 228.1-2021. Metallic materials-Tensile testing-Part 1:Method of test at room temperature. Beijing: China Standards Press; 2021 [in Chinese]

[22] Xu Y, Wu B, Zheng B. Full-field geometric imperfection and effect on cross-section capacity of circular steel tubes. J Construction Steel Res 2023;201:107749.

[23] GB 50205-2020. Standard for acceptance of construction quality of steel structures. Beijing: China Planning Press; 2020 [in Chinese].

[24] American Institute of Steel Construction (ANS//AISC), ANS/AISC 341-16. Seismic Provisions for Structural Steel Buildings, Illinois, USA, 2016.

[25] K. Wei, F. Yuan, X. Shao, Z. Chen, G. Wu, X. He, High-speed multi-camera 3D DIC measurement of the deformation of cassette structure with large shaking table, Mechanical Systems and Signal Processing 177 (2022) 109273.

[26] Timoshenko S, Gere J. Theory of elastic stability (International student edition). McGREW - Hill international book company; 1963.

[27] X. Cheng, D. Duan, A. Ali, Y. Chen, Constitutive model for thin-walled H-sections bent about weak-axis considering local buckling, Structures 25 (2020) 56–71.

[28] X. Cheng, Chen yiyi, Hinge zone model of H-section steel members and hinge zone length. journal of tongji university 2016;44: 677-684 [in Chinese].

[29] X. Cheng, Cross-section Classification and Hysteretic Behavior of Non-plastic-hinge H-section Steel Beam-columns. Tongji University Press;2017.

[30] Shi Binghua, Common formulas for calculating the non-uniformity coefficient of shear stress distribution in typical cross-sections, Journal of Building Structures 1984;66-69[in Chinese].

[31] Jin Zhang, Research and application of performance-based seismic design method and performance evaluation criteria for multistory steel structures. Nanjing: Southeast university; 2023 [in Chinese].

[32] JGJ 101—2015. Specification for seismic test of buildings. Beijing: China Architecture & Building Press; 2015 [in Chinese].

[33] Y. Wu, S. Fan, H. Zhou, Y. Guo, Q. Wu, Cyclic behaviour of diagonally stiffened stainless steel plate shear walls with two-side connections: Experiment, simulation and design, Engineering Structures 268 (2022) 114756.

[34] Chen, B. Zheng, G. Shu, Classification criteria for austenitic stainless steel H-section under cyclic loading about major-axis, Journal of Constructional Steel Research 214 (2024) 108460.

[35] Shi Y, Wang M, Wang Y. Experimental study of structural steel constitutive relationship under cyclic loading. J Build Mater 2012;15:293–300 [in Chinese].

[36] Suzuki Y, Lignos DG. Development of loading protocols for experimental testing of steel columns subjected to combined high axial load and lateral drift demands near collapse. Proc., 10th National Conf. on earthquake engineering. Anchorage, AK: Earthquake Engineering Research Institute; 2014.